Integrating Materials and Manufacturing Innovation (2021) 10:488–507
https://doi.org/10.1007/s40192-021-00229-0

TECHNICAL ARTICLE

Crystal Plasticity Finite Element Modeling of Extension Twinning in WE43 Mg Alloys: Calibration and Validation

Mohammadreza Yaghoobi[1] · Zhe Chen[2] · Veera Sundararaghavan[3] · Samantha Daly[2] · John E. Allison[1]

Received: 30 March 2021 / Accepted: 15 August 2021 / Published online: 7 September 2021

Abstract

Crystal plasticity simulation is an important tool for advanced Integrated Computational Materials Engineering for metals and alloys. The current work presents a calibration and validation framework for crystal plasticity finite element (CPFE) simulation of extension twinning in the Mg alloy WE43 using the scanning electron microscopy with digital image correlation (SEM-DIC) technique. Rolled Mg alloy WE43 was subjected to in situ uniaxial compression along its rolling direction. Full-field displacement maps were captured using SEM-DIC during load pauses, and twin variant maps were obtained from the strain maps using post-processing analysis. CPFE was used to investigate the experimental results via a multi-scale twinning model developed for HCP polycrystals. In addition to macroscopic stress–strain curves, crystal plasticity parameters were calibrated using the variation of twin fraction area versus the applied strain obtained from the SEM-DIC results to accurately capture the twinning parameters. A new SEM-DIC pipeline was created for the open-source PRISMS-Plasticity CPFE software that can read in the precise deformation map generated by SEM-DIC as an input boundary condition for the finite element simulation and conduct the CPFE simulation. The performance of CPFE was evaluated versus the SEM-DIC obtained strain and twin maps. The results show that the CPFE can successfully model the macroscopic stress–strain response and the twin area fraction and that it can additionally capture microscale strain and twinning.

Keywords Crystal plasticity finite element · Twinning · Digital image correlation · PRISMS-Plasticity · Deformation mechanisms · Magnesium

Introduction

Compared to other structural alloy systems, the development of commercial Mg alloys and understanding of Mg alloy physical metallurgy are less mature. Mg alloys have significant potential for reducing the weight of automobiles and other transportation systems, and thus for improving fuel economy and reducing emissions [1]. Many of these potential applications require significant improvements in strength, formability, and fatigue resistance. Achieving any of these goals requires a better understanding of the deformation mechanisms of Mg alloys. Twinning is an important deformation mechanism in Mg alloys, as in many HCP metals and alloys [2–8]. The slip mode of basal $\langle a \rangle$ is the easiest deformation mode to activate, but this cannot occur during tensile deformation along the c-axis. In this case, extension twinning $\{10\bar{1}2\}\langle\bar{1}011\rangle$ becomes the governing deformation mechanism. Extension twinning also becomes dominant during compression loading parallel to the basal plane. The activation of twinning in these special orientations leads to the highly asymmetric response of Mg alloys. The effects of sample microstructure on twinning mechanisms have been investigated in several studies [3, 9–15]. The studies describe twin nucleation and growth in Mg alloys using different attributes, such as the nominal Schmid factor and characteristics of the neighboring grains.

Crystal plasticity is an effective Integrated Computational Materials Engineering (ICME) tool for investigating deformation, including twinning, in metals and alloys [16–30]. Studies have shown that crystal plasticity can successfully capture the asymmetry observed in Mg alloy behavior.

✉ Mohammadreza Yaghoobi
yaghoobi@umich.edu

[1] Materials Science and Engineering, University of Michigan, Ann Arbor, MI 48109, USA

[2] Mechanical Engineering, University of California at Santa Barbara, Santa Barbara, CA 93106, USA

[3] Aerospace Engineering, University of Michigan, Ann Arbor, MI 48109, USA

Different crystal plasticity schemes have captured twinning in polycrystals including crystal plasticity finite element (CPFE) [17, 19, 21, 24, 26, 29, 31–34], Taylor-type models [27], viscoplastic self-consistent (VPSC) [25, 35–37], elastic viscoplastic self-consistent (EVPSC) [38, 39], and elastoviscoplastic FFT formulation [40], a Taylor-type-FE multiscale framework [41, 42], and the VPSC-FE multiscale method [43–45]. Kalidindi [17] and Staroselsky and Anand [31] developed rate-dependent and rate-independent CPFE frameworks, respectively, which include twinning in addition to the slip mechanisms. In the case of Mg and its alloys, Fernández et al. [20, 22] and Liu and Wei [23] have successfully modeled twinning in Mg and its alloys using the rate-independent CPFE framework. Abdolvand and his coworkers [19, 46, 47] incorporated a twin model into a rate-dependent CPFE framework based on the approach developed by Kalidindi [17]. Hama et al. [33] incorporated twinning into the CPFE framework to model the anisotropic response of Mg alloy sheets subjected to two-step loading. Plane strain CPFE was used by Prasad et al. [34] to capture ductile fracture in pure Mg using a model that captures both slip and twinning. Yaghoobi et al. [8] implemented twinning into the rate-independent CPFE framework to capture the uniaxial response of extruded Mg alloy ZK60A. Some advanced CPFE models have also been developed to capture new aspects of twinning in polycrystals including explicit twin lamella [24] and stress relaxation [26].

Most crystal plasticity simulations are calibrated and evaluated using the macroscale responses obtained from experiment and not the microscale deformation mechanisms. Although these studies showed the accuracy of the macroscale results, there is no guarantee that they can uniquely capture the microscale response of the sample. Advances in experimental techniques have enabled the evaluation of crystal plasticity models using microscale information. One of these techniques is synchrotron X-ray diffraction, which has been alternatively called high-energy diffraction microscopy (HEDM) or three-dimensional X-ray diffraction (3DXRD). Synchrotron X-ray diffraction provides valuable microscale information that has been recently used to calibrate and validate crystal plasticity simulations (Shade et al. [32, 48–53]). Twinning mechanisms have been investigated using synchrotron X-ray experiments [49, 54, 55]. Abdolvand et al. [32, 49, 56] investigated the deformation twinning in Zircaloy-2 and AZ31B Mg alloy using synchrotron X-ray diffraction experiments and CPFE. They compared the average stress for each grain obtained by experiment and CPFE simulation [32, 49, 56]. In the case of AZ31B Mg alloy, they also investigated the effect of crystallographic orientations on twin formation [32]. Pagan et al. [51] investigated the elastic strain tensor in individual grains of Ti alloy using HEDM and CPFE and studied the strength of individual slip systems and their contribution to the total response of the sample. Wang et al. [52, 57] investigated the strength of slip systems in pure Ti and Mg-Y alloy. They incorporated viscoplastic self-consistent (VPSC) modeling along with HEDM to investigate the deformation mechanisms of Mg-Y [52]. Greeley et al. [53] investigated the evolution of deformation mechanisms in Mg-Nd alloy using HEDM in conjunction with CPFE.

In addition to synchrotron X-ray experiments, digital image correlation (DIC) (see, e.g., Sutton et al. [58, 59], Kammers and Daly [60]) is another technique that can provide local deformation data to evaluate the crystal plasticity simulations. The SEM-DIC technique has been successfully applied to Mg alloys. Martin et al. [61] incorporated DIC based on SEM images over an area of $800 \times 800\ \mu m^2$ and a full-field viscoplastic fast Fourier transform (VPFFT) crystal plasticity simulation to study the response of a ZEK100 Mg alloy at the microscale. Githens et al. [62] investigated the deformation mechanisms of WE43 Mg alloy in the T5 condition during uniaxial tension using SEM-DIC technique and CPFE simulation. Paudel et al. [63] incorporated optical microscopy and strain fields from the DIC analysis over an area of $6.2 \times 5.18\ mm^2$ along CPFE to investigate twinning during three-point bending in AZ31 and ZEK100 Mg alloys. They showed that the twin bands formed in a strongly textured AZ31 alloy, but were not observed in the ZEK100 Mg alloy [63]. Ganesan et al. [64] investigated the effects of heat treatment on the mechanical response of a WE43 Mg alloy using the combination of SEM-DIC experiment and CPFE simulation. Githens et al. [62, 64] did not, however, extract twin maps and twin area fraction and were thus not able to compare the twinning observed in experiment and simulation. They incorporated a simple phenomenological predominant twin reorientation scheme (PTR) scheme-based model into the CPFE simulation [62, 64] to capture the twinning behavior. This model neglected the contribution of stress inside the twin itself to slip and twinning. Furthermore, the model did not consider stress relaxation associated with twinning. SEM-DIC provides the spatial strain and twin maps, while HEDM generates the grain level strain and twin information. Although the SEM-DIC and HEDM experiments provide different types of data, both provide a mean to evaluate the crystal plasticity simulations using the local response, rather than a macroscopic evaluation.

In addition to slip parameters, twinning parameters must be calibrated in the crystal plasticity modeling of twinning. They can be calibrated using the stress–strain responses for loading along different directions, especially in directions where twinning is the dominant deformation mechanism [17, 19, 21, 24, 26, 29, 31–34]. Twin fraction is commonly reported as a crystal plasticity simulation result. Some works have investigated either the change in the normalized intensity of the {0002} diffraction peak obtained in the experiment [8, 65], or reported twin fraction directly [39, 66]. The

twin fraction variation can be used as a measure of model accuracy, and also as a means to calibrate the crystal plasticity models. Chen and Daly [67–69] developed an SEM-DIC experimental framework that can identify twinned regions with high fidelity across large fields of view. The results from this method provide a consistent framework to calibrate the twinning parameters of crystal plasticity models.

In the present work, a calibration and validation framework is presented for the CPFE simulation of extension twinning using SEM-DIC experimental data. The CPFE simulation was incorporated to model twinning in WE43 Mg alloy, and both twin area fraction and local twin maps were investigated as macroscale and microscale measures, respectively. SEM-DIC was first used to calibrate the CPFE model using the experimentally obtained total twin fraction and then used to evaluate the CPFE in comparison with experimental strain and twin maps. The sample had weak basal texture along the rolling direction (RD), and twinning was an important deformation mechanism during uniaxial compression along the RD. The SEM-DIC technique provided the full-field displacement maps at different globally applied strains. Analytical techniques developed by Chen and Daly [67–69] were incorporated to generate twin maps by post-processing the experimental displacement data. The multiscale physically based twin–detwin CPFE framework developed by Yaghoobi et al. [8] was incorporated to capture twinning; this model can include the stresses both inside the parent grain and within the twinned child at each material point. Since the applied loading was monotonic, no detwinning occurred, and the original model was simplified by removing the detwinning terms. The CPFE parameters were calibrated using both the uniaxial tensile and compression responses and the twinned area obtained from SEM-DIC. An SEM-DIC pipeline was developed for the open-source CPFE software PRISMS-Plasticity [29, 70] which can read in the SEM-DIC displacement map as an input, extract the CPFE simulation boundary conditions from that input, and conduct the CPFE simulation. The local fields including strain and twin maps obtained by SEM-DIC experiment were then used to evaluate the CPFE simulation.

Material and Experimental Methods

The material investigated in this study was a rare earth containing Mg alloy, WE43, in the T6 condition. The as-received material was provided by Magnesium Elektron Ltd. as hot rolled plate in the T5 condition. The as-received T5 material was subsequently solution-treated at 525 °C for eight hours, followed by water quenching. The material was then peak-aged at 250 °C for 16 h to obtain the T6 condition. Flat dog bone-shaped specimens were cut from the rolled plate by electrical discharge machining. The loading direction was parallel to the rolling direction (RD) of the plate, and the sample normal direction (ND) was parallel to the normal direction of the plate. The specimen gage was 10 mm long × 3.5 mm wide × 3.5 mm thick. The specimen was ground and polished with SiC paper, diamond paste, and finished with MaterPolish™ alumina and silica suspension (Buehler, Lake Bluff, IL). The specimen was then etched with a mixture of 50 ml methanol, 6 ml hydrochloric acid, and 4 ml nitric acid to characterize the pre-deformation microstructure by electron backscatter diffraction (EBSD). After that, the specimen surface was patterned with 300-nm diameter gold nanoparticles following the method of [71, 72].

To investigate deformation at the microstructural length scale, *in situ* testing was performed in a FEI Teneo scanning electron microscope (SEM). Compressive loading was applied using a Kammrath & Weiss miniature stage with a constant displacement rate of 1 µm/s. The test was paused at several globally applied strain levels of − 0.003, − 0.004, − 0.012, − 0.023, and − 0.039, and SEM images were captured using a customized system for automated multi-tile imaging [68]. At each pause, a grid of 11 × 19 images, each with 4096 × 4096 pixel resolution and 360 × 360 µm field of view size, was captured to cover the area of interest. The full-field displacements and Lagrangian strains were measured by DIC from individual images and stitched [68]. To perform DIC, a commercial software Vic-2D 6 (Correlated Solutions, Inc., Irmo, SC) was used, with a subset size of 21 pixels and a step size of 5 pixels. A portion of the results from this experiment have been previously published in order to describe the development of the SEM-DIC technique [68] and machine learning enabled twin identification [67, 69]. However, in the current work, the results are presented in full and elaborated in detail for the first time in order to both examine the microscale features of twinning and calibrate and validate the developed CPFE framework in capturing both macroscopic response, such as stress–strain, twin area evolution, and slip activity, as well as the microscale details of strain and twinning.

Simulation Methodology

Crystal Plasticity Model

The response of the WE43-T6 alloy was modeled using a multiscale rate-independent single crystal plasticity theory developed by Yaghoobi et al. [8]. The selected crystal plasticity model is based on the finite deformation continuum mechanics framework. This model incorporates a multiscale homogenization scheme to track the evolution of both untwinned and twinned regions, which are called parent and child, respectively, following the terminology

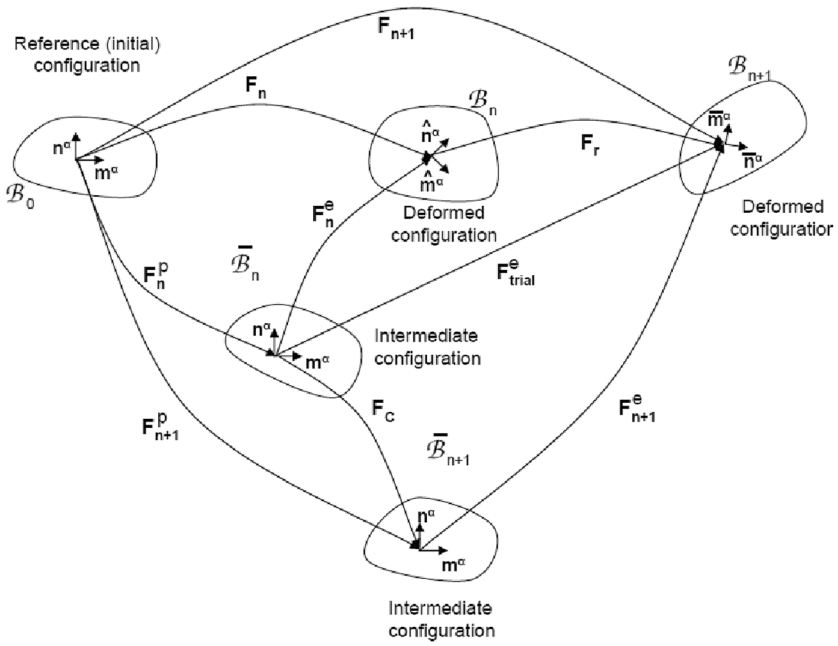

Fig. 1 Schematic of the various material configurations, for a single crystal, used in the integration of the constitutive model. The slip systems (m^α, n^α) are known in the reference (initial) configuration. Also, $\hat{m}^\alpha$ and $\dot{m}^\alpha$ are the slip directions (different from m^α because of crystal re-orientation) in the deformed configurations $\bar{\varkappa}_n$ and $\bar{\varkappa}_{n+1}$, respectively (reprinted from Computational Materials Science, Vol. 169, M. Yaghoobi, S. Ganesan, S. Sundar, A. Lakshmanan, S. Rudraraju, J.E. Allison, V. Sundararaghavan, PRISMS-Plasticity: An open-source crystal plasticity finite element software, 109078, (2019), with permission from Elsevier)

of Yaghoobi et al. [8]. In the following formulations, the superscripts *mt* and *tw*, *k* correspond to the parent and child nucleated due to the activation of k^{th} twin system of the parent, respectively.

In the case of the multiscale twin model, the response of a material point including both parent and children is homogenized using the Taylor model by assuming that both regions undergo the same deformation gradient tensor **F**. In the case of finite strain plasticity, the additive decomposition of strains is no longer valid, and the elastic and plastic deformations are related through the multiplicative decomposition of the deformation gradient tensor as follows (see, e.g., Voyiadjis and Yaghoobi [73] and Yaghoobi et al. [29]):

$$\mathbf{F} = \mathbf{F}^{e^{mt}}\mathbf{F}^{p^{mt}} = \mathbf{F}^{e^{tw,k}}\mathbf{F}^{p^{tw,k}} \tag{1}$$

where $\mathbf{F}^{\mathrm{e}}$ and $\mathbf{F}^{\mathrm{p}}$ are the elastic and plastic deformation gradient tensors, respectively. Figure 1 presents the kinematics of single crystal slip for both twinned and untwinned regions, in which the superscripts are dropped. In Fig. 1, different configurations are presented from time = t_n to t_{n+1}. $\boldsymbol{\beta}_0$ represents the undeformed configuration, $\boldsymbol{\beta}_n$ and $\boldsymbol{\beta}_{n+1}$ denote the deformed body at time = t_n and t_{n+1}, respectively, and $\bar{\boldsymbol{\beta}}_n$ and $\bar{\boldsymbol{\beta}}_{n+1}$ represent the intermediate configurations at time = t_n and t_{n+1}, respectively. As shown in Fig. 1, the plastic deformation gradient $\mathbf{F}^{\mathrm{p}}$ transforms the elemental vector in the undeformed body to the intermediate state. Next, the elastic deformation gradient $\mathbf{F}^{\mathrm{e}}$ transforms the elemental vector in the intermediate state to that of the deformed body. All the following equations in this section are described in the deformed configuration.

The macroscopic velocity gradient tensor **L** can be decomposed into two mechanisms, elastic distortion of the crystal lattice and pure shear as a result of plastic slip, as follows:

$$\mathbf{L} = \mathbf{L}^{\mathrm{e}^{mt}} + \mathbf{L}^{\mathrm{p}^{mt}} = \mathbf{L}^{\mathrm{e}^{tw,k}} + \mathbf{L}^{\mathrm{p}^{tw,k}} \tag{2}$$

where L^e and L^p are the elastic and plastic velocity gradient tensors, respectively. The key idea of crystal plasticity is to link the macroscopic response (plastic part of the velocity gradient) to the microscopic deformation mechanisms (superposition of shear deformation induced by crystallographic slip on multiple crystallographic systems) as below:

$$\mathbf{L}^{\mathrm{p}^{mt}} = \sum_{\alpha=1}^{N_s^{mt}+N_t^{mt}} \dot{\gamma}^\alpha \mathbf{S}^\alpha \mathrm{sign}(\tau^\alpha) \tag{3}$$

$$\mathbf{L}^{\mathrm{p}^{tw,k}} = \sum_{\beta=1}^{N_s^{tw}+N_t^{tw}} \dot{\bar{\gamma}}_k^\beta \mathbf{S}_k^\beta \mathrm{sign}\left(\tau_k^\beta\right) \tag{4}$$

where the twinning systems are modeled as pseudo-slip systems. τ^α, $\dot{\gamma}^\alpha$, and S^α are the resolved shear stresses, shearing rate, and Schmid tensor, respectively, on slip systems α in a parent grain. τ_k^β, $\dot{\bar{\gamma}}_k^\beta$, and S_k^β are the resolved shear stresses, shearing rate, and Schmid tensor, respectively, on β^{th} system of the k^{th} child. N_s^{mt} and N_t^{mt} are the number of slip and twinning pseudo-slip systems in a parent. N_t^{mt} includes both twin growth and twin shrinkage. N_s^{tw} and N_t^{tw} are the number of slip and twinning pseudo-slip systems in children. In the current model, $N_t^{tw} = 2$ including one for twin growth and one for twin shrinkage inside a child.

The resolved shear stress is calculated from the Cauchy stress tensor $\boldsymbol{\sigma}$ as follows:

$$\tau^{\alpha} = \boldsymbol{\sigma}^{mt} : \mathbf{S}^{\alpha} \tag{5}$$

$$\tau_k^{\beta} = \boldsymbol{\sigma}_k^{tw} : \mathbf{S}_k^{\beta} \tag{6}$$

As a last component of a rate-independent crystal plasticity model, the yield surface is defined using the resolved shear stress and slip resistance s as follows:

$$g^{\alpha} = |\tau^{\alpha}| - s^{\alpha} \tag{7}$$

$$g_k^{\beta} = \left|\tau_k^{\beta}\right| - s_k^{\beta} \tag{8}$$

The slip resistance in parent and child is evolved as follows:

$$\dot{s}^{\alpha} = \sum_{\vartheta} h^{\alpha\vartheta}\dot{\gamma}^{\vartheta} \tag{9}$$

$$\dot{s}_k^{\beta} = \sum_{\varphi} h_k^{\beta\varphi}\dot{\bar{\gamma}}_k^{\varphi} \tag{10}$$

where $h^{\alpha\vartheta}$ and $h_k^{\beta\varphi}$ are the hardening moduli of the parent and child, respectively. A power-law relationship is used to capture the combined effects of work hardening and recovery as follows:

$$h^{\alpha\vartheta} = \begin{cases} h_0^{\vartheta}\left[1 - \frac{s^{\vartheta}}{s_s^{\vartheta}}\right]^{a^{\vartheta}} & \text{if } \alpha = \vartheta \left(\text{coplanar systems}\right) \\ h_0^{\vartheta} q\left[1 - \frac{s^{\vartheta}}{s_s^{\vartheta}}\right]^{a^{\vartheta}} & \text{if } \alpha \neq \vartheta \end{cases} \tag{11}$$

where q is the latent hardening ratio, h_0^{ϑ} denotes the initial hardening parameter, s_s^{ϑ} is the saturation slip resistance, and a^{ϑ} is a material constant that controls the sensitivity of the hardening moduli to the slip resistance.

The model is able to capture the lattice reorientation during deformation. The polar decomposition of elastic deformation gradient F^e can be described as follows:

$$\mathbf{F}^{\mathrm{e}} = \mathbf{R}^{\mathrm{e}}\mathbf{U}^{\mathrm{e}} \tag{12}$$

where $\mathbf{R}^{\mathrm{e}}$ and $\mathbf{U}^{\mathrm{e}}$ are the rotation and material stretch tensors, respectively. The elastic asymmetric spin tensor $\boldsymbol{\omega}^{\mathrm{e}}$ can be derived using the elastic rotation tensor as follows:

$$\boldsymbol{\omega}^{\mathrm{e}} = \dot{\mathbf{R}}^{\mathrm{e}}\mathbf{R}^{\mathrm{e}^T} \tag{13}$$

The grain orientations are updated from their initial orientations by integrating Eq. (9).

A Taylor-type homogenization scheme is used to capture the response of a twinned material point. Accordingly, the homogenized Cauchy stress tensor $\boldsymbol{\sigma}$ is described as follows:

$$\boldsymbol{\sigma} = \left(1 - f_{tw}\right)\boldsymbol{\sigma}^{mt} + \sum_{k=1}^{n_t^{mt}} f_{tw}^k \boldsymbol{\sigma}_k^{tw} \tag{14}$$

where f_{tw} is the total fraction of the reoriented children nucleated due to twinning, i.e., $f_{tw} = \sum_{k=1}^{n_t^{mt}} f_{tw}^k$, f_{tw}^k is the twin fraction of the reoriented child nucleated due to the activation of k^{th} twin system of the parent, and n_t^{mt} is the number of nucleated children.

Twinning Model

The multiscale rate-independent CPFE model presented by Yaghoobi et al. [8] can capture both twinning and detwinning mechanisms by defining four mechanisms including: (I) twin nucleation followed by twin growth due to parent shrinkage (operation A); (II) twin growth due to the child propagation (operation B); (III) twin shrinkage due to the parent propagation (operation C), and (IV) detwinning inside the child (operation D). Although detwinning can be important for cyclic loading situations, detwinning is not expected in samples subjected to uniaxial compression. Accordingly, out of the described four operations, only operations *A* and *B* are active during uniaxial compression and studied in the current work (Fig. 2). The evolution of twin fraction can be described by incorporating the operations *A* and *B* as follows:

$$\dot{f}_{tw}^{\kappa *} = \left[1 - f_{tw}\right]\frac{\dot{\gamma}^{N_s^{mt}+k}}{S} + f_{tw}^{\kappa}\frac{\dot{\bar{\gamma}}_k^{N_s^{tw}+2}}{S} \tag{15}$$

where S is the characteristic twin shear strain, which is calculated as 0.129 in the case of Mg [74], $\dot{\gamma}^{N_s^{mt}+k}$ is the shear rate of $\left(N_s^{mt}+k\right)^{th}$ system inside the parent that corresponds to operation *A*, and $\dot{\bar{\gamma}}_k^{N_s^{tw}+2}$ is the shear rate of $\left(N_s^{tw}+2\right)^{th}$ system inside the child nucleated due to the activation of k^{th} twin system of the parent, which corresponds to the operations *B*. In this model, after the twin fraction of f_{tw}^{k*} reaches a critical value of f_0, the child is created by lattice reorientation of parent according to the k^{th} twin system, and $\dot{f}_{tw}^{k}$ and f_{tw}^{k} become equal to $\dot{f}_{tw}^{k*}$ and f_{tw}^{k*}. The twin can grow due to the parent reduction which occurs when $\tau^{N_s^{mt}+k} > s^{N_s^{mt}+k}$ (operation *A*). Also, a twin can grow due to the child propagation which occurs when $\tau_k^{N_s^{tw}+2}\langle 0$ and $\left|\tau_k^{N_s^{tw}+2}\right|\rangle s_k^{N_s^{tw}+2}$ (operation *B*).

The evolution of total twin fraction f_{tw} can be defined as:

$$\dot{f}_{tw} = \sum_{k=1}^{n_t^{mt}} \dot{f}_{tw}^{k} \tag{16}$$

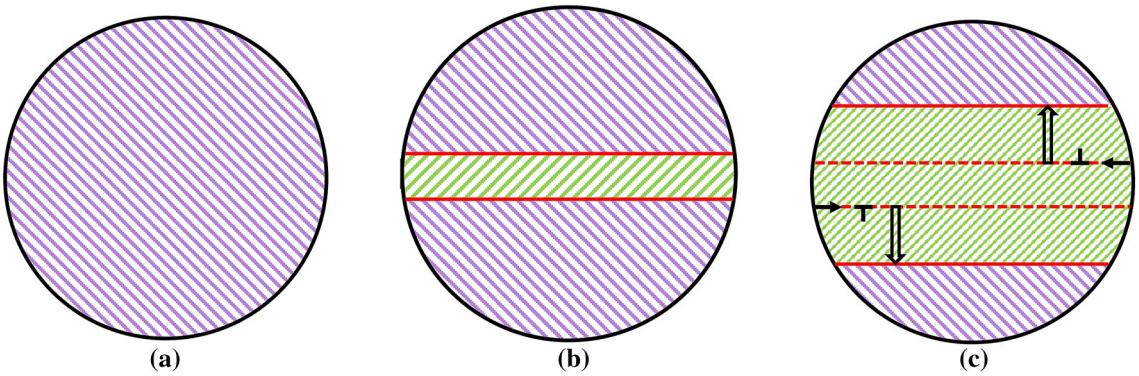

Fig. 2 The schematic of twinning mechanisms in a material point: **a** The material point is initially twin-free, which is called the parent; **b** *Operation A:* The twin nucleation occurs when the twin fraction reaches a critical value of f_0. The nucleated twin can grow due to the parent reduction. **c** *Operation B:* The twin grows due to the child propagation

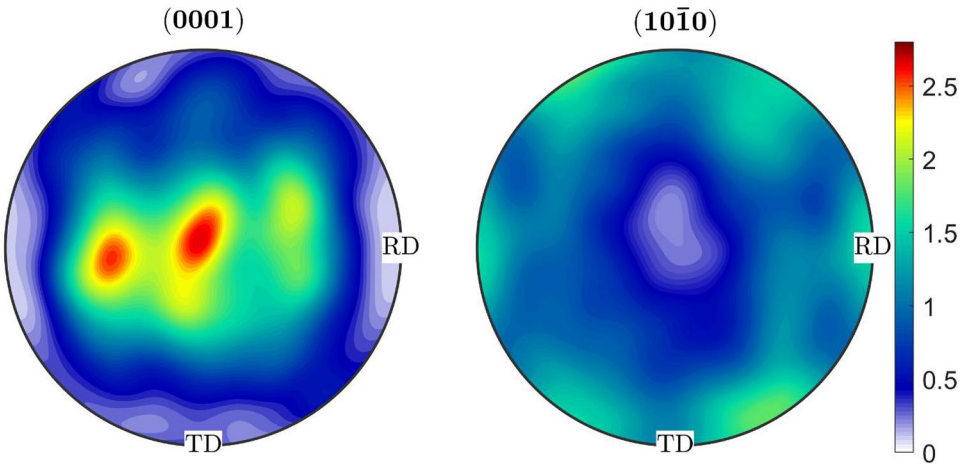

Fig. 3 (0001) and (10$\bar{1}$0) pole figures showing the initial texture of rolled WE43-T6 Mg alloy

where n_t^{mt} is the number of children nucleated due to twinning with a twin fraction larger than f_0. The rate-independent model is implemented in the open-source CPFE software, PRISMS-Plasticity [29], as described in Yaghoobi et al. [8]. The twinning model can handle two different types of simulation. First, each material point represents a volume large enough to include multiple twin variants. Second, a high-resolution simulation can be conducted in which only a small fraction of a grain is represented by each material point. In this case, to reduce the computational cost, one can merely model one active twin system at each material point as a reasonable simplification. Consequently, a criterion is added to the model in which all twin variants initially evolve until one of them reaches a threshold of f_0, at which point twinning in other variants is prohibited. In other words, each material point may have a parent and maximum of one child, in which the child twin fraction is governed according to Eq. (11). One should note that although the FE mesh seems very fine, as will be discussed later, the spatial resolution of the SEM-DIC map is much higher. In the finest FE simulation reported in the current work, each FE mesh represents 36 SEM-DIC voxels. As shown later in the experimental twin maps, the twin features are extremely fine, i.e., the twinned region frequently consists of very thin bands. Accordingly, each FE material point can potentially include both twinned and non-twinned regions, which was the main motivation for including both twinned and untwinned regions in a material point.

Results and Discussion

Mechanical Properties

The undeformed basal and prismatic pole figures of the WE43-T6 sample are illustrated in Fig. 3. The microstructure contained equiaxed grains with an average grain diameter of 116 µm. The material exhibited a moderately weak texture, where the basal poles showed a maximum intensity about four times of random in the sample ND. A slight split

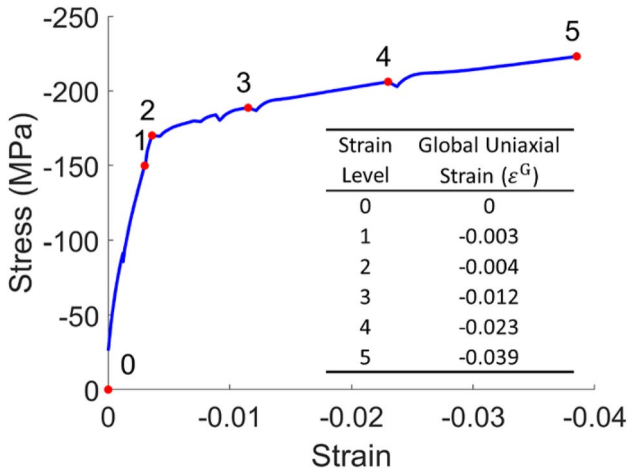

Fig. 4 Engineering stress–strain curve for the loading processing during in situ compression test. The red dots indicate the strain levels at which the test was paused for imaging (reprinted with minimal modification from Materials Science and Engineering A, vol. 736, Z. Chen, S. Daly, Deformation twin identification in magnesium through clustering and computer vision, 61–75, (2018), with permission from Elsevier)

of the basal pole intensity toward the RD was also observed. The prismatic poles exhibited a sixfold symmetry where higher intensities about two times of random were observed in the sample RD.

The engineering stress–strain curve for the *in situ* compression testing is shown in Fig. 4. The red dots indicate the strain values at which the test was paused for imaging. The strain values were calculated by averaging the axial strain (ε_{xx}) values of all data points in the investigated area analyzed by DIC. Strain level 2 was close to the point of global yielding, and strain levels 3–5 were in the plastic regime of the loading process.

The axial strain (ε_{xx}) maps at different global strain (ε^G) values are shown in Fig. 5. At strain level 1 ($\varepsilon^G = -0.003$), fine slip traces were observed in a number of grains, and there were no obvious instances of twinning observed. This is reasonable considering the relatively weak texture of the sample, where a large portion of grains may be oriented such that basal slip is favored. Twinning started to be observed at strain level 2 ($\varepsilon^G = -0.004$). The number of twinned grains and the twinning area kept increasing with the increased magnitude of global compressive strain. A strong

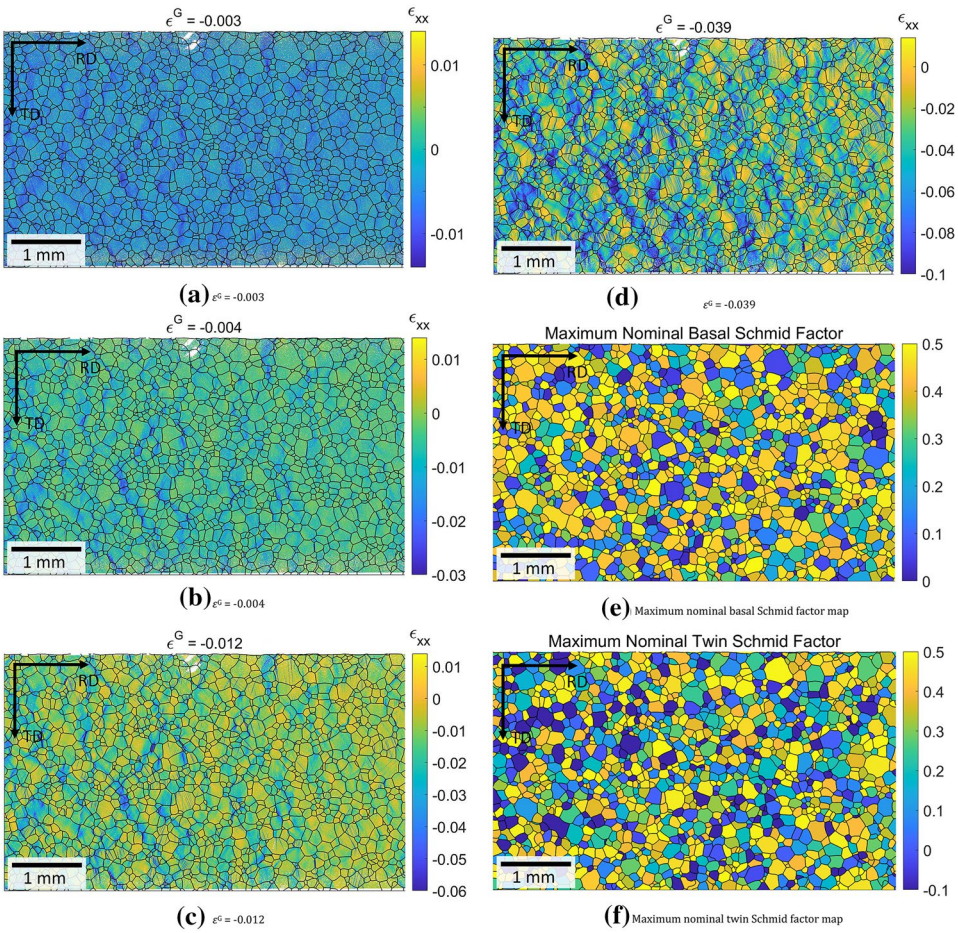

Fig. 5 Axial strain (ε_{xx}) map of the WE43-T6 sample at different global strain (ε^G) values during in situ compression test: **a** $\varepsilon^G = 0.003$, **b** $\varepsilon^G = -0.004$, **c** $\varepsilon^G = -0.012$, **d** $\varepsilon^G = -0.039$; **e** maximum nominal basal Schmid factor map; **f** maximum nominal twin Schmid factor map

heterogeneity can be observed on the strain map. For grains that exhibited slip traces, the strain magnitude appeared to increase during the loading process, and the strain magnitude in certain grains appeared to be significantly higher and concentrated. For the twinned grains, the twin area grew with increased global strain, but the non-twinned area in these grains exhibited very low strain magnitudes.

Deformation Twinning Identification

Deformation twinning in the WE43-T6 sample was identified using full-field microscale strain data, and the procedure described by Chen and Daly [67–69]. Data points for each grain were first segmented into different clusters corresponding to connected areas within a grain, based on the three components (ε_{xx}, ε_{xy}, ε_{yy}) of the strain tensor. Then, each cluster was either identified as a non-twinned area, or a twinned area of a specific variant of the extension twinning, by a combined consideration of the strain value of the cluster, the geometry/shape of the area of the cluster, and the comparison of cluster area at different strain levels. The twin variant map of the sample at different global strain levels is shown in Fig. 6. The six variants of the $\{10\bar{1}2\}\langle\bar{1}011\rangle$ extension twinning were determined, and different variants of the identified deformation twins were marked by different colors. Note that twinning was confidently not observed at strain level 1 ($\varepsilon^G = -0.003$), so the twin variant map at this strain level is not shown. At the highest magnitude of global strain of $\varepsilon^G = -0.039$, about 25% of the grains were observed to contain twins. For grains that exhibited twinning, most of them had only one or two twin variants activated.

Each twin variant map was divided into 12 smaller sections, and the twin area fraction was obtained for each section. The average twin area fraction and the corresponding error bar were generated using the data of each smaller section at each strain, as shown in Fig. 7. It is observed that the twin area percent increased nearly linear with the global compressive strain.

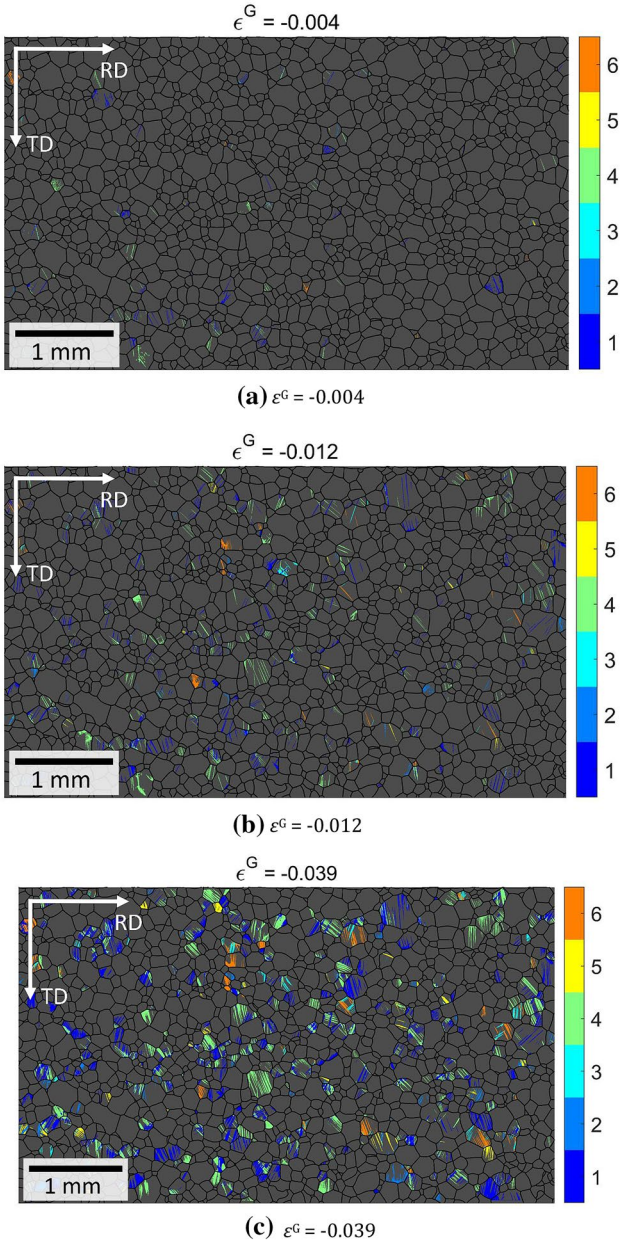

Fig. 6 Deformation twinning variant map of the WE43-T6 sample at different global strain (ε^G) values during in situ compression test: **a** $\varepsilon^G = -0.004$, **b** $\varepsilon^G = -0.012$, **c** $\varepsilon^G = -0.039$. Note that no twinning was identified with confidence at strain level 1 ($\varepsilon^G = -0.003$)

PRISMS-Plasticity Simulation of SEM-DIC Experiment

An important and unique capability of PRISMS-Plasticity and other full-field CPFE simulation software is the ability to simulate arbitrary applied boundary conditions rather than symmetric ones. To exploit this capability, an automated pipeline was established for extracting SEM-DIC displacements for use as boundary conditions in PRISMS-Plasticity. The uniaxial compressive response of WE43-T6 alloy was modeled using four slip modes of Basal a ($\{0001\}\langle11\bar{2}0\rangle$), Prismatic a ($\{10\bar{1}0\}\langle11\bar{2}0\rangle$), Pyramidal a ($\{10\bar{1}1\}\langle11\bar{2}0\rangle$), and Pyramidal c + a ($\{\bar{1}\bar{1}22\}\langle\bar{1}\bar{1}23\rangle$), along one extension twin mode ($\{10\bar{1}2\}\langle\bar{1}011\rangle$). In order to simulate the sample during uniaxial compression, the boundary value problem was set up similar to Githens et al. [62] by using the EBSD image of the microstructure within the DIC window as the simulation microstructure. In order to mimic the SEM-DIC experiment, a pipeline was developed for PRISMS-Plasticity (Fig. 8). The SEM-DIC pipeline is integrated in the

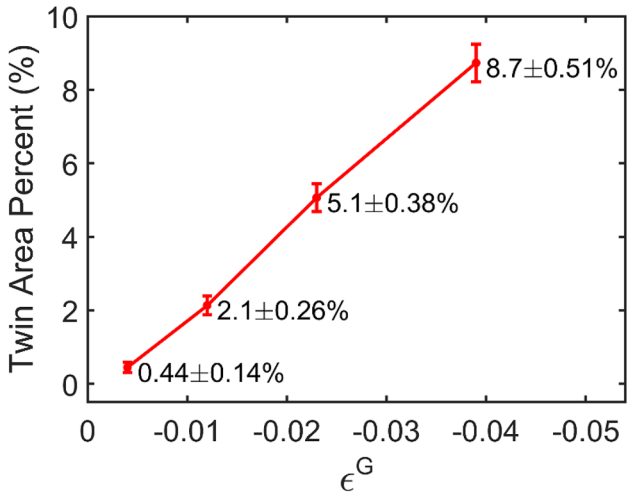

Fig. 7 Twin area percent of the sample at different global strain levels

in Githens et al. [62], the DIC displacements were measured on the traction-free surface of the sample, and therefore, a generalized plane-stress assumption was made while setting up the simulation. The slip and twin systems are three-dimensional, and the algorithm to solve for the shear strains and stresses in the slip systems proceeds from a 3-D deformation gradient. Therefore, it was not possible to set up an explicit plane-stress problem similar to 2-D elasticity. Instead, the problem was set up in 3-D with a plate with a small thickness-to-length ratio of 0.1. Since no variation of variables u and v was expected in the z -direction, a single layer of elements was assumed in the z -direction along with a 500×400 mesh in x–y plane. Githens et al. [62] compared the results of the generated columnar sample versus 3D sample and showed that a choice of generalized plane-stress on a columnar grain structure can mimic the SEM-DIC experiment since the surface is traction free.

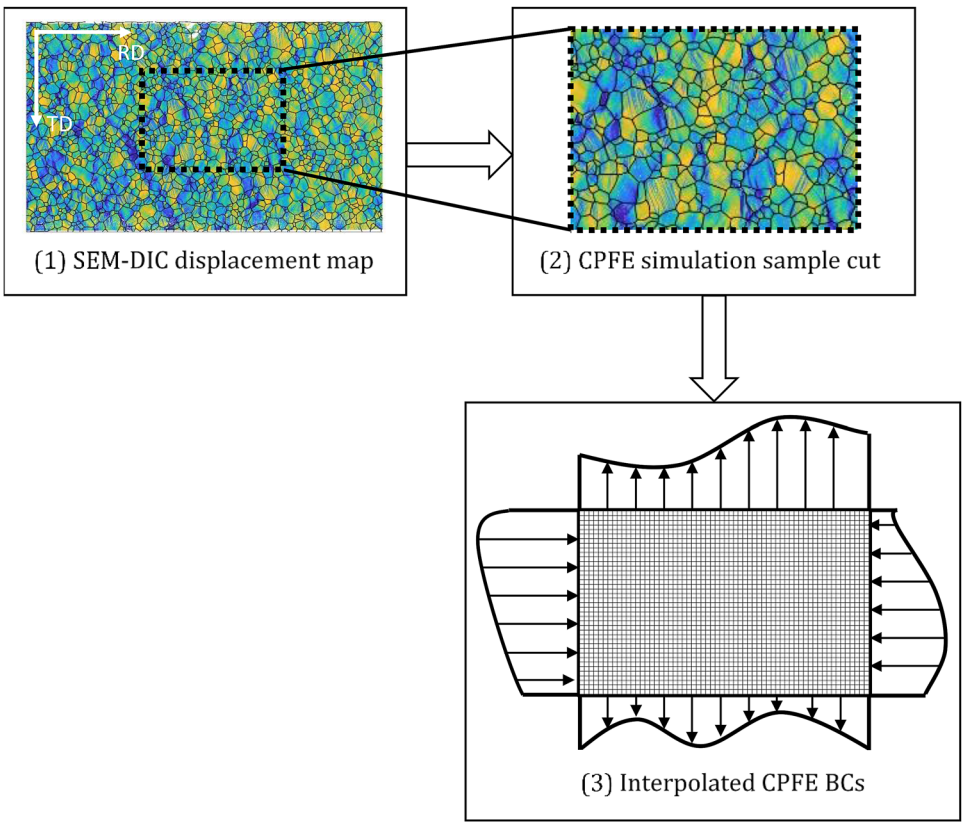

Fig. 8 The SEM-DIC pipeline designed for PRISMS-Plasticity. This pipeline can read in the SEM-DIC displacement map and extract the precise CPFE boundary conditions using the linear interpolation

PRISMS-Plasticity software package on GitHub as a new feature (See Appendix). This pipeline reads in the displacement map from the SEM-DIC experiment and extracts the spatially resolved external boundary conditions for the selected simulated sample. The linear interpolation was applied to external nodes to extract the boundary conditions from the experimental displacement map. As detailed

Calibration of Crystal Plasticity Parameters

The rate-independent crystal plasticity model was first calibrated using the uniaxial compression and tension responses of the WE43-T6 sample. In addition to the stress–strain curves of the WE43-T6 sample, the twin area fraction variation

Table 1 The elastic constants (MPa) of pure Mg at room temperature

C11	C12	C13	C33	C44
59,400	25,610	21,440	61,600	16,400

Table 2 The calibrated values of initial slip resistance and corresponding hardening parameters for slip and twining modes of WE43-T6 Mg alloy

Mode	s_0^α (MPa)	h_0^α (MPa)	s_s^α (Mpa)	a^α
Basal	47.6	250	144.4	2.5
Prismatic	92.2	350	289.0	2.5
Pyramidal < a >	104.5	350	347.5	2.5
Pyramidal < c + a >	117.3	350	304.9	2.5
Twinning < c + a >	93	1000	350	2.5
Twinning (children)	85	1000	320	2.5

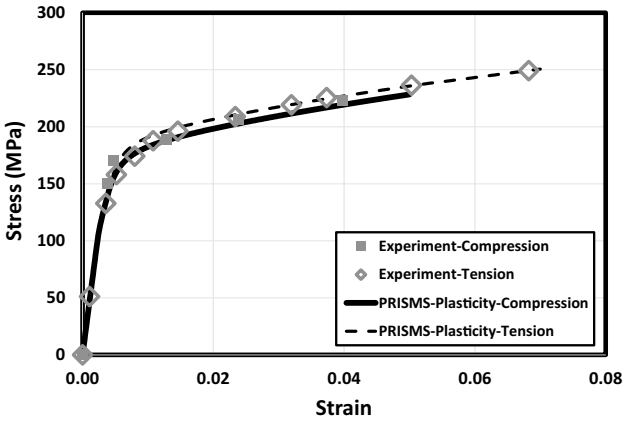

Fig. 9 The responses of WE43-T6 alloy sample during uniaxial tension and compression loadings along the extrusion direction. The experimental responses are compared versus the PRISMS-Plasticity simulation results

versus strain during uniaxial compression was used for further calibration. Since the twin area fraction should be also calibrated, a boundary value problem was set up using the EBSD image of the microstructure within the DIC window as the simulation microstructure. Several simulations were conducted to calibrate the model. Accordingly, a coarser FE discretization of 100×100 was used with the simple uniaxial compression and tension boundary conditions along RD for the calibration of the PRISMS-Plasticity model. The elastic constants of pure Mg at room temperature (Zhang and Joshi [21]; Yaghoobi et al., [8]) were incorporated and are presented in Table 1. Ganesan et al. [64] calibrated the WE43-T6 Mg alloy for uniaxial compression and tension. However, twinning area data were not available in their work, and accordingly, they did not calibrate their model using that data. Also, Ganesan et al. [64] used a predominant twin reorientation (PTR)-based scheme developed by Tomé et al. [16]. Unlike the PTR method in which only one twin mechanism is defined, in the current scheme two twin mechanisms contribute to the twinning model, and two sets of parameters should be calibrated that correspond to operations *A* and *B* as discussed in Sect. 3.2. Some relaxation due to twin nucleation is considered here associated with the decrease in critical stress between operations *A* and *B*. The CPFE parameters were calibrated by a gradient optimization approach starting from the material parameters of WE43-T6 alloy calibrated by Ganesan et al. [64] for uniaxial compression and tension by adding the twin area variation into the consideration. The calibration results show that the final crystal plasticity model parameters, including the initial and saturation CRSS, latent hardening ratio, and hardening exponent a^ϑ, were similar to those calibrated by Ganesan et al. [64] for different slip systems. The twin parameters CRSS and the initial hardening values h_0^ϑ were slightly adjusted to accommodate the changes due to the new twin model and further calibration of twin area fraction versus strain during compression. Table 2 presents the crystal plasticity parameters for slip and twinning modes. As described by Qiao et al. [65] and Yaghoobi [8], the CRSS for operation *A* was selected higher than that of operation *B*, which can mimic the stress relaxation due to twinning. The latent hardening ratio $q = 1.4$ was used for slip deformation according to the Ganesan et al. [64]. In the case of latent hardening ratio for the twinning, following Qiao et al. [65] and Yaghoobi et al. [8], the latent hardening ratio q was selected to be one for operations *A* and *B*. Figure 9 compares the experimental stress–strain curves for uniaxial tension and compression versus the CPFE simulation. The CPFE can successfully capture the stress–strain response of the WE43-T6 alloy under both applied uniaxial compression and tension. The variation in the experimentally obtained twin area fraction of the specimen as the strain increased during uniaxial compression was in good agreement with the CPFE results (Fig. 10a). In addition to the total twin fraction area, the contributions of operations A and B, i.e., respectively, to twin area fraction are plotted in Fig. 10b. The results show that neglecting the child role in twin growth will underestimate the twinning activation.

In order to study the effect of twinning on texture evolution, the evolution of pole figures during uniaxial compression and tension was examined. Figure 11a,b shows the predicted evolution of (0001) pole figures from the initial texture (Fig. 11a) to the final texture (Fig. 11b) of the simulated WE43-T6 sample at a compressive strain of 5% along RD. The twinning mechanism leads to the reorientation of the basal pole; accordingly, the part of texture with the c-axis normal to RD axis undergoes a 86.3° reorientation (see, e.g., Yaghoobi et al. [8]) which leads to an increase in the basal {0002} peak intensity in the loading direction at the end of compressive loading along RD. In order to further

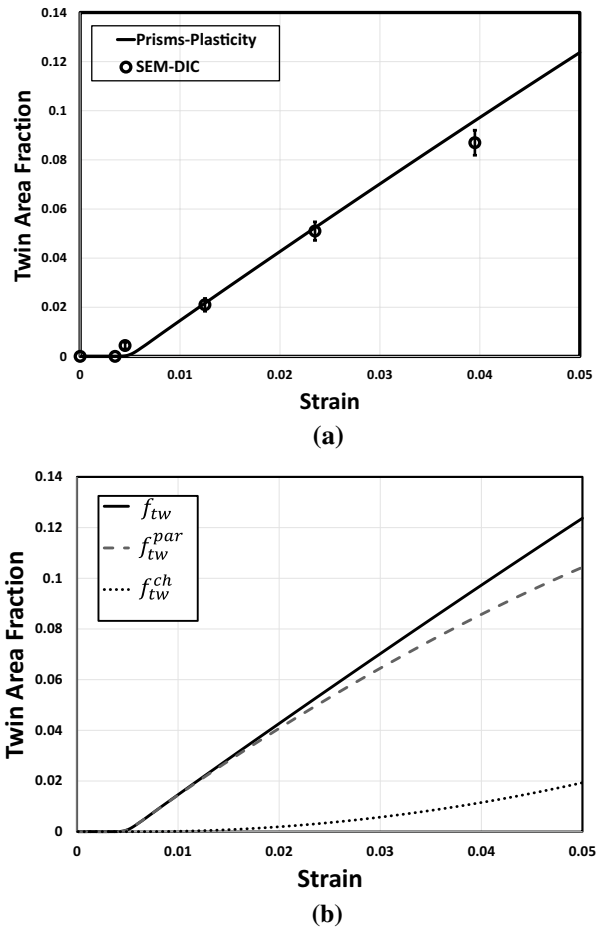

Fig. 10 The evolution of twin area fraction in WE43-T6 alloy during uniaxial compression along RD: **a** comparison of the PRISMS-Plasticity simulation results versus the experimental data; **b** contributions of parent and children in twinning fraction, i.e., f_{tw}^{par} and f_{tw}^{ch}, respectively, obtained from PRISMS-Plasticity simulation

investigate the evolution of texture, the difference in the (0001) pole figures of initial texture and deformed sample is presented in Fig. 11c. Twin reorientation is the main factor producing the texture evolution, which is represented by the zone of the pole figures along the RD orientation with the intensity difference in the region of $0.5 - 0.8$. However, the texture also evolved due to the lattice reorientation during the deformation induced by the contribution of slip modes, especially basal and prismatic, which is represented in these pole figures as a zone with the intensity difference in the region of $0 - 0.5$. Figure 12 shows the predicted evolution of (0001) pole figures in the simulated WE43-T6 sample during the uniaxial tension parallel to the RD orientation. Since there is limited twinning during tensile loading, the lattice reorientation is primarily driven by basal and prismatic slip modes. One can see that the difference in intensity of the pole figure represented in Fig. 12c is mostly in the range of $0 - 0.5$, which is in line with the changes in the intensity of the pole figures during compressive deformation driven by basal and prismatic slip modes. However, unlike the compressive loading, there is almost no region on the difference in the pole figures with the intensity range of $0.5 - 0.8$ during the tensile loading, which is in line with the low extension twinning activity during uniaxial tension.

The relative activity of deformation modes is presented in Fig. 13 for a simulated WE43-T6 sample under uniaxial compression and tension loadings. The relative activity of a deformation mode is defined here as the ratio of the total shear strain due to that deformation mode over the total plastic shear accumulated in the microstructure. Basal slip has the lowest CRSS and is the most active deformation mechanism at low strain levels for both uniaxial tension and compression. In the case of uniaxial compression (Fig. 13a), as the sample begins to macroscopically yield, extension twinning and prismatic modes become active and have a key role in the response of the sample. At higher compressive strains, the role of pyramidal $\langle c + a \rangle$ becomes considerable. In the case of uniaxial tension (Fig. 13b), the prismatic and pyramidal $\langle c + a \rangle$ plays a key role as the sample begins to macroscopically yield. Unlike uniaxial compression, the contribution of extension twinning is negligible for uniaxial tension. This is in line with the texture evolution results presented in Figs. 11 and 12.

Comparison of SEM-DIC and CPFEM

The experimental SEM-DIC results of WE-43 T6 alloy during compression along RD were compared with the CPFE simulation obtained using PRISMS-Plasticity. The spatially resolved boundary conditions were applied to the simulated sample using the developed SEM-DIC pipeline for PRISMS-Plasticity. Figure 14 compares the ε_{xx} strain maps of SEM-DIC versus the CPFE simulation at compressive strains of $-0.003, -0.004, -0.012, -0.023$, and -0.039 along the RD. The results show that CPFE can capture the general

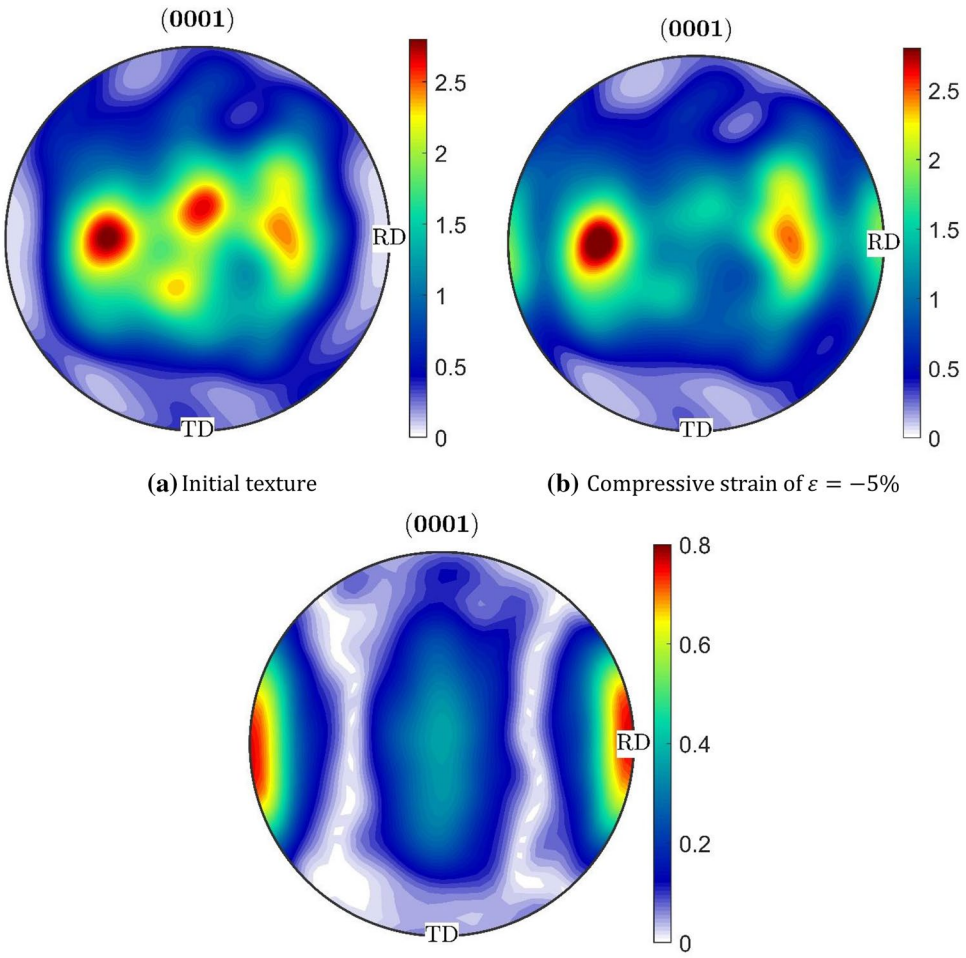

Fig. 11 The predicted evolution of basal (0001) pole figures in the simulated WE43-T6 sample during uniaxial compression along RD: **a** initial texture; **b** compressive strain of $\varepsilon = -5\%$; **c** difference between the initial and deformed sample

(a) Initial texture

(b) Compressive strain of $\varepsilon = -5\%$

(c) Difference between the initial and deformed sample

heterogeneity of the strain and can also model some of the localized strain traces. However, some localized strain traces smeared out in the CPFE simulation.

In order to quantitatively compare the results of SEM-DIC and CPFE, the ε_{xx} strain was averaged for each grain at the strain of -0.039 and investigated. The average weighted error (considering the grain size as the weight) in the simulated sample is 20.54%. Figure 15 compares the error in CPFE prediction of ε_{xx} compared to the SEM-DIC data over all grains versus the relative grain area $\left(A^{\text{Grain}}/A^{\text{Average}}\right)$ and maximum nominal basal Schmid factor. As the grain size increases, the error decreases (Fig. 15a). The smaller errors for larger grains can be attributed to the fact that the current formulation does not include the effect of the grain boundary strain gradient. Accordingly, regions close to the grain boundary are more prone to have a larger discrepancy compared to the SEM-DIC values. However, further away from the grain boundary, this effect becomes less important. In the case of larger grains, a smaller portion of the grain will be affected by the grain boundary which leads to the lower error in the CPFE prediction. In very small grains, however, almost the entire grain is influenced by the grain boundary which leads to the higher errors due to the absence of any grain boundary strain gradient in the current model. There was no correlation between the nominal basal Schmid factor and the observed errors, as shown in Fig. 15b.

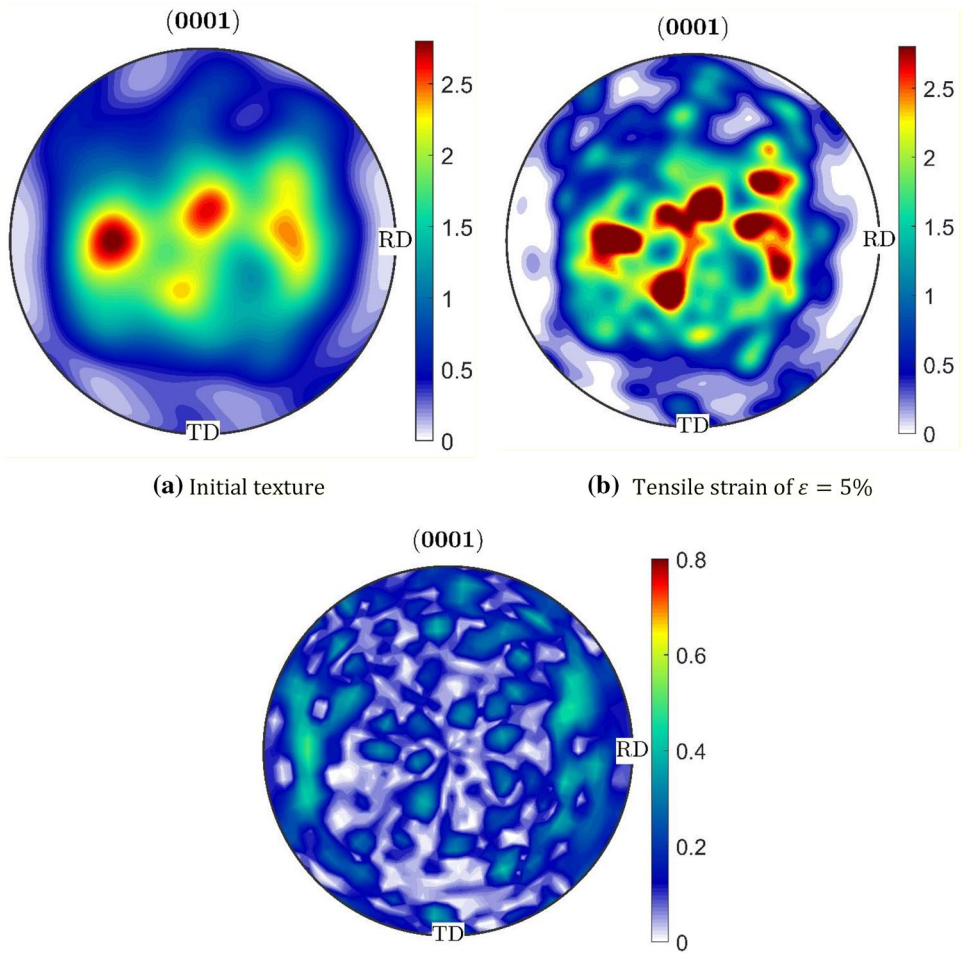

(a) Initial texture

(b) Tensile strain of $\varepsilon = 5\%$

(c) Difference between the initial and deformed sample

Fig. 12 The predicted evolution of basal (0001) pole figures in the simulated WE43-T6 sample during uniaxial tension along RD: **a** initial texture; **b** tensile strain of $\boldsymbol{\varepsilon} = 5\%$; **c** difference between the initial and deformed sample

In addition to strain maps, the twin maps are compared between the SEM-DIC and CPFE as shown in Fig. 16 at the compressive strain of -0.039 along RD. Unlike the SEM-DIC data, in which a material point is either twinned or not, the CPFE simulation considers the parent grain and twinned child to coexist at each material point, while the fraction of twin child increases as the compressive strain increases. Figure 16a shows the twin variants map obtained from the SEM-DIC, while Fig. 16b shows the CPFE twin fraction area map. In the CPFE framework presented by Yaghoobi et al. [8], a threshold must be defined for an initial twin volume fraction. Above that threshold, the material point can be considered as twinned. In the current work, this threshold is defined as 20% by comparing the simulated twin maps versus the SEM-DIC twin maps. However, the contribution of the non-twinned portions will continue as a correction factor for better capturing both macroscopic and local strain distributions. Accordingly, the material points with twinned child fraction higher than 20% are considered as twinned in Fig. 16b. Comparing Fig. 16a and b, the results show that the twin model in PRISMS-Plasticity can capture the general pattern of twinning. The sharp twin bands are smeared out in CPFE, as there is no explicit rule for the formation of the twins as narrow bands. Even without implementation of any strict rules for twin shape formation, some of the sharp twin bands are captured by CPFE (e.g., Grain G). Figure 16c and

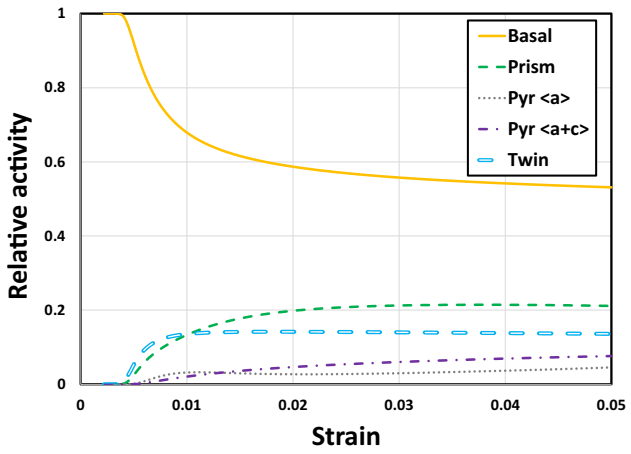

(a) Uniaxial compression

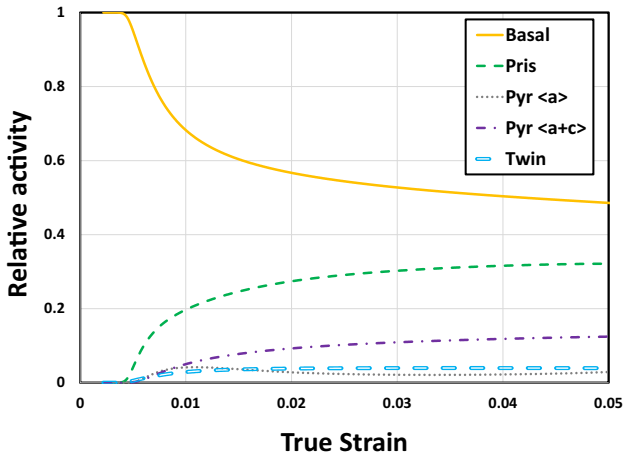

(b) Uniaxial tension

Fig. 13 The predicted relative activities of slip and twin modes of simulated WE43-T6 sample during uniaxial loading along RD: **a** uniaxial compression; **b** uniaxial tension

d shows the maps for maximum nominal Schmid factors for both basal and twinning modes, respectively. Maximum nominal Schmid factor for basal (twin) is calculated among the 3 basal (6 twin) variants. Comparing Fig. 16a and b with Fig. 16c and d, one can see that grains with high twinning and low apparent basal Schmid factors clearly have a better chance of twinning (such as grains A, B, and C), which was also captured by CPFE. However, twinning in a grain with a high apparent basal Schmid factor and low apparent twin Schmid factor (such as grains D, E, and F) is less likely. Twinning also was found to occur in a grain with intermediate apparent basal and twin Schmid factors (grain G), as shown in the SEM-DIC twinning map of Fig. 16a and captured by the CPFE simulation. The results show that CPFE can capture the twinning in grains which are favored for twinning (Such as grains A, B, and C), and it can also accurately model the neighborhood effect and capture twinning in grains with intermediate apparent twin and basal Schmid factors that are not favored for twinning (grain G).

One should note the connection and differences between the results presented in Figs. 15 and 16. The fact that there is an error in predicted grain level strains (Fig. 15) is not in contradiction the success of the simulation for predicting the local extension twinning (Fig. 16). During uniaxial compression, the extension twinning mechanism is the governing deformation mechanism in grains with low maximum nominal basal Schmid factors. The basal mode, however, is the controlling deformation mechanism in grains with high maximum nominal basal Schmid factors. As the results in Fig. 15b show, there is no correlation between the observed errors in the grain level strain prediction and the maximum nominal basal Schmid factor. Accordingly, no correlation between the observed errors and the governing deformation mode, including twinning, was observed. In other words, if the error in the predicted grain level strain was due to the inaccuracy of the twinning prediction, it should be increased by decreasing the maximum nominal basal Schmid factor, which is not the case. Consequently, the error in the grain level strain prediction observed in Fig. 15 cannot be attributed to an error in the extension twinning prediction. In the current simulation, the largest source of error in the prediction of grain level strain was observed to be the effect of grain size and the contribution of grain boundaries to the deformation mechanisms, which is an ongoing research activity.

To further demonstrate the capabilities of the developed framework, another section of the SEM-DIC surface was simulated using the developed SEM-DIC pipeline. The results were compared to those of the experimental data in WE43-T6 alloy sample at the compressive strain of -0.039 along RD, as shown in Fig. 17. The boundary conditions were applied to the simulated sample using the developed SEM-DIC pipeline for PRISMS-Plasticity which reads in the precise SEM-DIC boundary displacements. Figure 17a and b compares the strain maps predicted by CPFE simulation and extracted from the SEM-DIC experiment, respectively. The results show that CPFE can capture the general heterogeneity of the strain. However, CPFE smears most

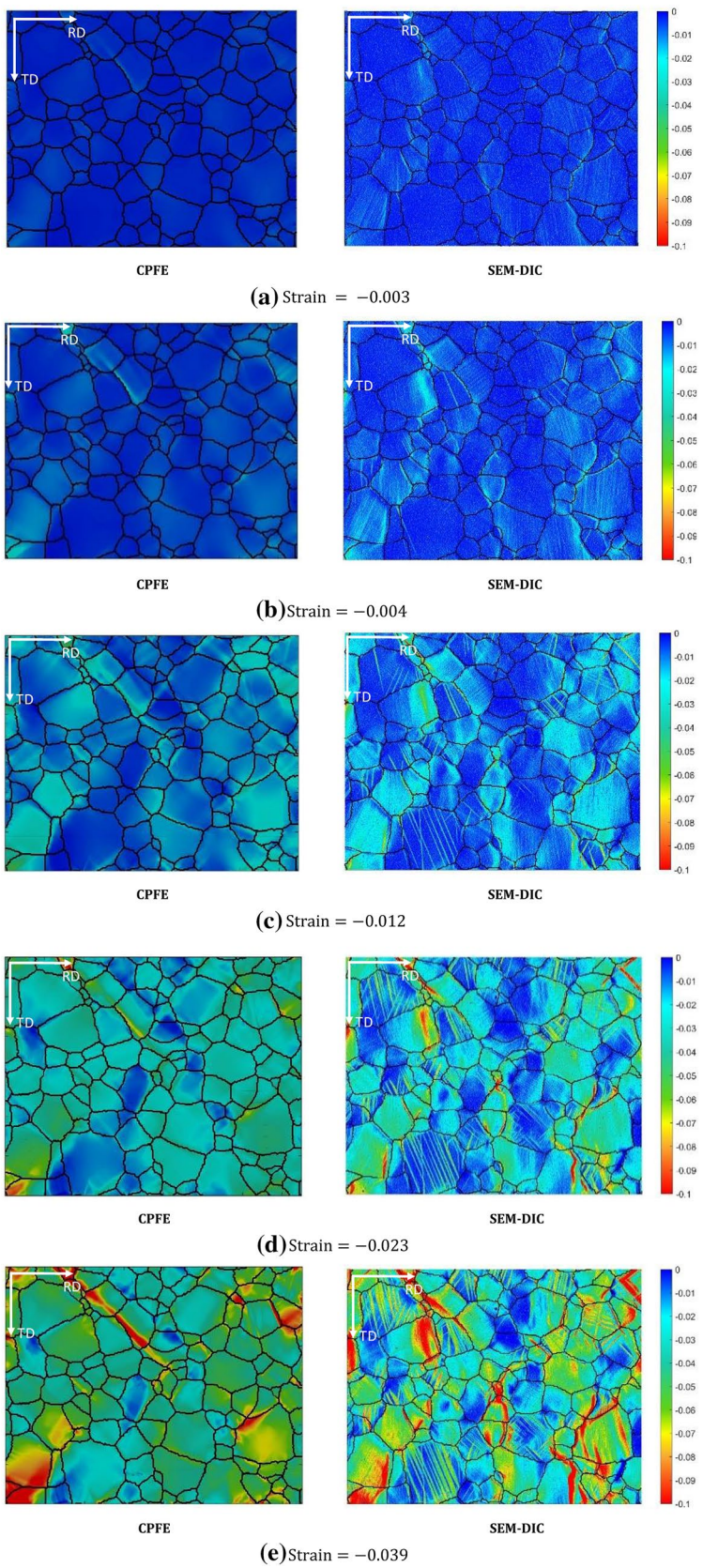

Fig. 14 The ε_{xx} strain maps comparison of SEM-DIC versus the PRISMS-Plasticity simulation in WE43-T6 alloy sample during the uniaxial compression along RD at different compressive strains of: **a** – 0.003; **b** – 0.004; **c** – 0.012; **d** – 0.023; **e** – 0.039. The SEM-DIC strain maps are located on the left, while CPFE simulation results are on the right

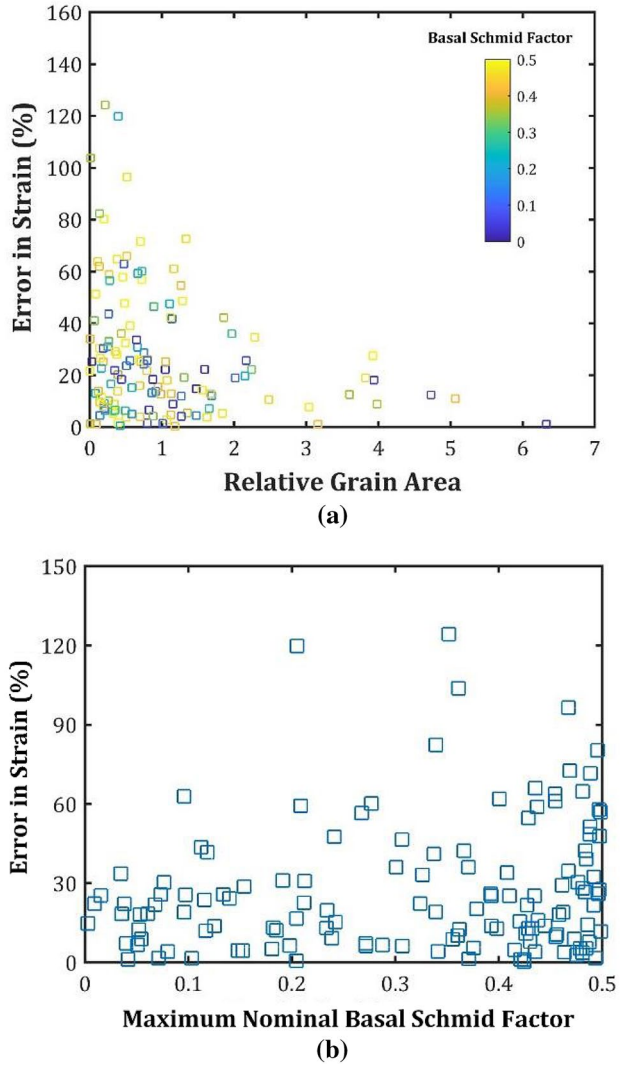

Fig. 15 The error in CPFE prediction of ϵ_{xx} as a function of: **a** relative grain area $\left(A^{Grain}/A^{Average}\right)$; **b** maximum nominal basal Schmid factor. The strain values are averaged over each grain in WE43-T6 alloy sample at the compressive strain of – 0.039 along RD

of the sharp localized strain bands. The twin maps are compared between the CPFE and SEM-DIC as shown in Fig. 17c and d, respectively, at the compressive strain of -0.039 along RD. The CPFE accurately predicts more than 80% of the twinned grains but was unable to precisely capture the twin morphology.

Comparing Figs. 16a, b and 17c, d, one can see that the twin morphology predicted by the CPFE simulation does not exactly match with that of SEM-DIC, as CPFE largely smears the twin bands. This discrepancy can be attributed to the fact that conventional continuum crystal plasticity does not have any tool to govern twin morphology directly and tends to smear twin bands independent of the twinning scheme. One can assign external crystallographic constraints to model the twin bands or even explicitly model them within the microstructure (see, e.g., Ardeljan et al. [24]). Although these models present twin bands qualitatively, to the best of the authors' knowledge, they have never been compared directly with experimental twin maps, and their limitations have not been investigated. The only possible alternative is to couple the phase field simulation with the CPFE simulation (Kondo et al. [75], Liu et al. [76], Liu et al. [77], Ma and Sun [78]). While the CPFE handles the stress by solving the equilibrium equations, the phase-field simulation governs the twin nucleation and growth. Again, these models qualitatively investigated the effects of twin bands so far, and to the best of the authors' knowledge, they have never been compared directly with experimental twin maps, and thus, their limitations are unknown. The aim of the current study is to investigate the local twinning obtained by CPFE simulation and study the capabilities and limitations of the CPFE framework in capturing local twin response.

Summary and Conclusions

Twinning in rolled sheet Mg alloy WE43 was investigated using an integrated framework of SEM-DIC experimental data and PRISM-Plasticity CPFE simulation. The SEM-DIC twin area fraction was used to calibrate the twinning CRSS along with the experimental uniaxial stress–strain responses. The CPFE simulation results were then evaluated versus the SEM-DIC strain and twin maps. The major contributions and conclusions can be summarized as follows:

- The high-resolution, spatially resolved twin maps including the twin variants are obtained using SEM-DIC along

Fig. 16 Comparison of twinning observed in SEM-DIC experiment versus the CPFE simulation results in WE43-T6 alloy sample at the compressive strain of -0.039 along RD: **a** twin variant map of SEM-DIC experiment; **b** twin area fraction map of CPFE simulation; **c** maximum nominal basal Schmid factor map; **d** maximum nominal twin Schmid factor map

a novel post-processing scheme [67–69] for Mg alloy WE43 specimen with a weak basal texture subjected to the uniaxial compressive loading along RD leading to twinning of ~ 25% of grains.

- The multiscale physically based twin–detwin model developed by Yaghoobi et al. [8] was simplified here to the case of monotonic loading (i.e., no detwinning) to capture the twinning in WE43 alloy.
- Both stress–strain response and twin area fraction were used to calibrate the CPFE parameters. The calibrated parameters can be used for additional WE43-T6 samples as long as the microstructural features are similar to those reported here. If any of the microstructural features changes considerably, the calibrated values should be adjusted depending on the extent of the change.
- The importance of consideration of the twinned child role in twin modeling was demonstrated.
- A new pipeline was developed for PRISMS-Plasticity which reads in the deformation map generated by SEM-DIC and generates CPFE boundary conditions. This pipeline enhances the 2D simulation to represent the precise BCs applied to the specimen.
- The CPFE simulation results were evaluated by comparing the strain and twin maps obtained from SEM-DIC and CPFE. The results show that the model which was calibrated using the stress–strain data and twinning data obtained from SEM-DIC can successfully capture the observed patterns in local strain and twin maps observed in the SEM-DIC experiment. However, the results showed that the CPFE framework smears the spatial representation of strain and twin bands.
- The results show that CPFE can capture the twinning in grains which are favored for twinning, i.e., low nominal basal and high nominal twin Schmid factors. Importantly, it can also accurately model the neighborhood effect and capture twinning in grains with intermediate apparent twin and basal Schmid factors, which are not favored for twinning just by considering the nominal Schmid factor.

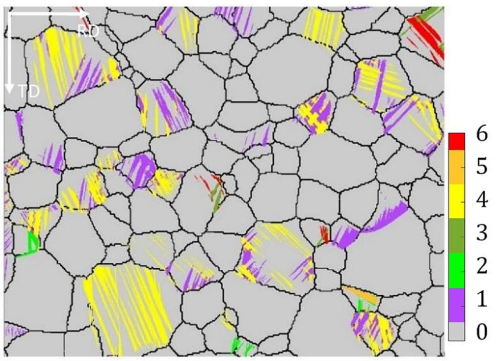

(a) SEM-DIC twin variants map

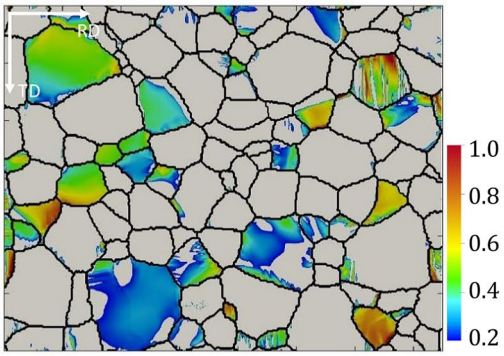

(b) CPFE twin area fraction map

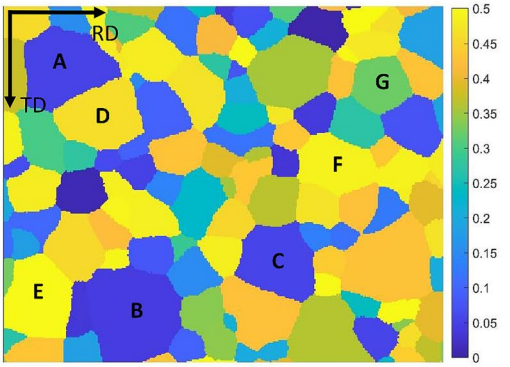

(c) Maximum nominal basal Schmid factor map

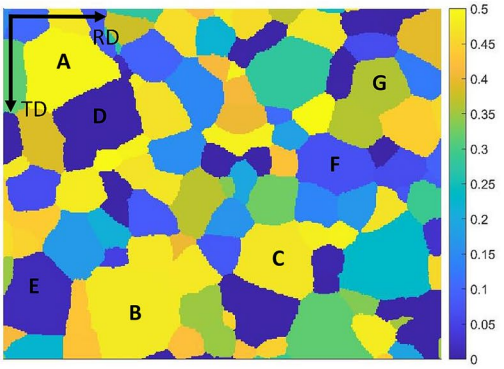

(d) Maximum nominal twin Schmid factor map

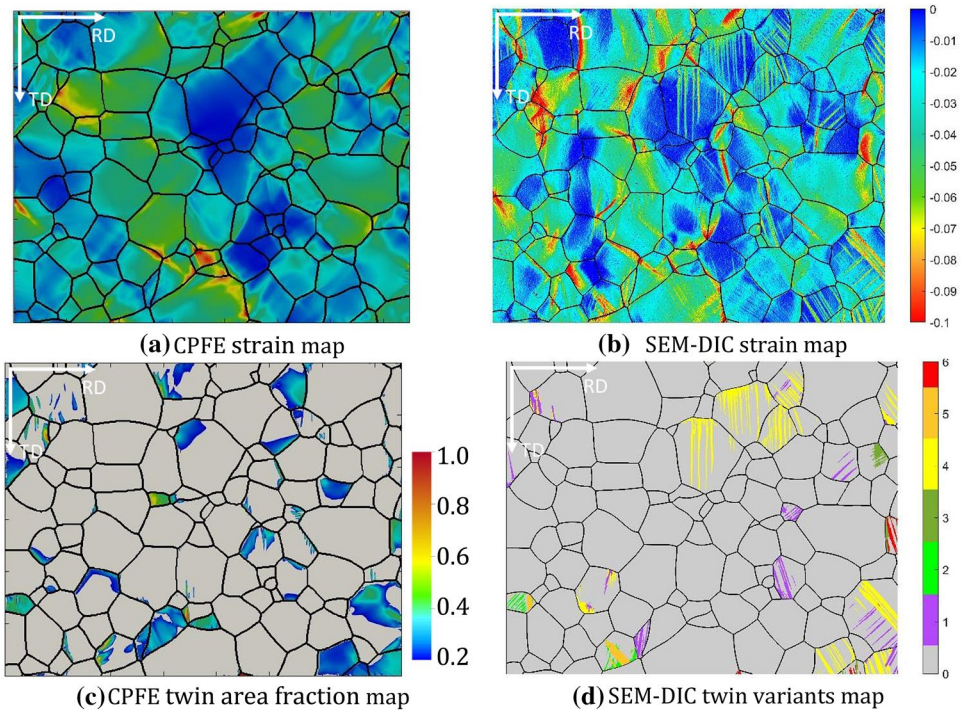

Fig. 17 Comparison of strain and twin maps observed in SEM-DIC experiment versus the CPFE simulation results in WE43-T6 alloy sample at the compressive strain of−0.039 along RD: **a** CPFE strain map; **b** SEM-DIC strain map; **c** CPFE twin area fraction map; **d** SEM-DIC twin variants map

Appendix

- PRISMS-Plasticity software can be freely downloaded from the following link: https://github.com/prisms-center/plasticity.
- SEM-DIC pipeline implementation for PRISMS-Plasticity can be found at: https://github.com/prisms-center/plasticity/tree/master/src/ellipticBVP/.

Acknowledgements This work was supported by the U.S. Department of Energy, Office of Basic Energy Sciences, Division of Materials Sciences and Engineering, under Award#DE-SC0008637 as part of the Center for Predictive Integrated Structural Materials Science (PRISMS Center) at University of Michigan. We also acknowledge the financial cost-share support of University of Michigan College of Engineering and Office of the Vice President for Research.

Data Availability The experimental data and PRISMS-Plasticity simulation input files and results are available on Materials Commons https://materialscommons.org/ and can be found at https://doi.org/10.13011/m3-thgc-jj93.

Declarations

Conflict of interest On behalf of all authors, the corresponding author states that there is no conflict of interest.

References

1. Cole GS (2016) Summary of "Magnesium vision 2020: a North American automotive strategic vision for magnesium." In: Essential readings in magnesium technology. Springer, pp 35–40
2. Begum S, Chen DL, Xu S, Luo AA (2009) Low cycle fatigue properties of an extruded AZ31 magnesium alloy. Int J Fatigue 31(4):726–735
3. Beyerlein IJ, Capolungo L, Marshall PE, McCabe RJ, Tome CN (2010) Statistical analyses of deformation twinning in magnesium. Phil Mag 90(16):2161–2190
4. Mirza FA, Chen DL, Li DJ, Zeng XQ (2013) Low cycle fatigue of a rare-earth containing extruded magnesium alloy. Mater Sci Eng A 575:65–73
5. Mokdad F, Chen DL (2015) Strain-controlled low cycle fatigue properties of a rare-earth containing ZEK100 magnesium alloy. Mater Des 67:436–447
6. Yu Q, Jiang Y, Wang J (2015) Cyclic deformation and fatigue damage in single-crystal magnesium under fully reversed strain-controlled tension-compression in the [1010] direction. Scripta Mater 96:41–44
7. Murphy-Leonard AD, Pagan DC, Beaudoin A, Miller MP, Allison JE (2019) Quantification of cyclic twinning-detwinning behavior during low-cycle fatigue of pure magnesium using high energy X-ray diffraction. Int J Fatigue 125:314–323
8. Yaghoobi M, Allison JE, Sundararaghavan V (2020) Multiscale modeling of twinning and detwinning behavior of HCP polycrystals. Int J Plast 127:102653
9. Capolungo L, Beyerlein IJ (2008) Nucleation and stability of twins in hcp metals. Phys Rev B 78(2):024117
10. Wang J, Hirth JP, Tomé CN (2009) (1^{-} 012) Twinning nucleation mechanisms in hexagonal-close-packed crystals. Acta Mater 57(18):5521–5530
11. Beyerlein IJ, Tomé CN (2010) A probabilistic twin nucleation model for HCP polycrystalline metals. Proceed Royal Soc A Math Phys Eng Sci 466(2121):2517–2544
12. Beyerlein IJ, McCabe RJ, Tomé CN (2011) Effect of microstructure on the nucleation of deformation twins in polycrystalline high-purity magnesium: a multi-scale modeling study. J Mech Phys Solids 59(5):988–1003

13. Zheng SJ et al (2012) Deformation twinning mechanisms from bimetal interfaces as revealed by in situ straining in the TEM. Acta Mater 60(16):5858–5866
14. Barrett CD, El Kadiri H (2014) The roles of grain boundary dislocations and disclinations in the nucleation of 1 0 1 2 twinning. Acta Mater 63:1–15
15. Beyerlein J, Arul Kumar M (2018) The stochastic nature of deformation twinning: application to HCP materials. In: Andreoni W, Yip S (eds) Handbook of materials modeling: methods: theory and modeling. Springer, Cham, pp 1–39
16. Tomé CN, Lebensohn RA, Kocks UF (1991) A model for texture development dominated by deformation twinning: application to zirconium alloys. Acta Metall Mater 39(11):2667–2680
17. Kalidindi SR (1998) Incorporation of deformation twinning in crystal plasticity models. J Mech Phys Solids 46(2):267–271
18. Staroselsky A, Anand L (2003) A constitutive model for hcp materials deforming by slip and twinning: application to magnesium alloy AZ31B. Int J Plast 19(10):1843–1864
19. Abdolvand H, Daymond MR, Mareau C (2011) Incorporation of twinning into a crystal plasticity finite element model: evolution of lattice strains and texture in Zircaloy-2. Int J Plast 27(11):1721–1738
20. Fernández A, Pérez Prado MT, Wei Y, Jérusalem A (2011) Continuum modeling of the response of a Mg alloy AZ31 rolled sheet during uniaxial deformation. Int J Plast 27(11):1739–1757
21. Zhang J, Joshi SP (2012) Phenomenological crystal plasticity modeling and detailed micromechanical investigations of pure magnesium. J Mech Phys Solids 60(5):945–972
22. Fernández A, Jérusalem A, Gutiérrez-Urrutia I, Pérez-Prado MT (2013) Three-dimensional investigation of grain boundary-twin interactions in a Mg AZ31 alloy by electron backscatter diffraction and continuum modeling. Acta Mater 61(20):7679–7692
23. Liu Y, Wei Y (2014) A polycrystal based numerical investigation on the temperature dependence of slip resistance and texture evolution in magnesium alloy AZ31B. Int J Plast 55:80–93
24. Ardeljan M, McCabe RJ, Beyerlein IJ, Knezevic M (2015) Explicit incorporation of deformation twins into crystal plasticity finite element models. Comput Methods Appl Mech Eng 295:396–413
25. Kabirian F, Khan AS, Gnäupel-Herlod T (2015) Visco-plastic modeling of mechanical responses and texture evolution in extruded AZ31 magnesium alloy for various loading conditions. Int J Plast 68:1–20
26. Qiao H, Barnett MR, Wu PD (2016) Modeling of twin formation, propagation and growth in a Mg single crystal based on crystal plasticity finite element method. Int J Plast 86:70–92
27. Lévesque J, Mohammadi M, Mishra RK, Inal K (2016) An extended Taylor model to simulate localized deformation phenomena in magnesium alloys. Int J Plast 78:203–222
28. Hama T, Kobuki A, Takuda H (2017) Crystal-plasticity finite-element analysis of anisotropic deformation behavior in a commercially pure titanium Grade 1 sheet. Int J Plast 91:77–108
29. Yaghoobi M et al (2019) PRISMS-plasticity: an open-source crystal plasticity finite element software. Comput Mater Sci 169:109078
30. Yaghoobi M, Voyiadjis GZ, Sundararaghavan V (2021) Crystal plasticity simulation of magnesium and its alloys: a review of recent advances. Crystals 11(4):435
31. Staroselsky A, Anand L (1998) Inelastic deformation of polycrystalline face centered cubic materials by slip and twinning. J Mech Phys Solids 46(4):671–673
32. Abdolvand H et al (2015) On the deformation twinning of Mg AZ31B: a three-dimensional synchrotron X-ray diffraction experiment and crystal plasticity finite element model. Int J Plast 70:77–97
33. Hama T, Tanaka Y, Uratani M, Takuda H (2016) Deformation behavior upon two-step loading in a magnesium alloy sheet. Int J Plast 82:283–304
34. Prasad NS, Narasimhan R, Suwas S (2017) Effects of lattice orientation and crack tip constraint on ductile fracture initiation in Mg single crystals. Int J Plast 97:222–245
35. Wang H, Raeisinia B, Wu PD, Agnew SR, Tomé CN (2010) Evaluation of self-consistent polycrystal plasticity models for magnesium alloy AZ31B sheet. Int J Solids Struct 47(21):2905–2917
36. Oppedal AL, El Kadiri H, Tomé CN, Vogel SC, Horstemeyer MF (2013) Anisotropy in hexagonal close-packed structures: improvements to crystal plasticity approaches applied to magnesium alloy. Phil Mag 93(35):4311–4330
37. Ostapovets A, Molnár P, Jäger A (2013) Visco-plastic self-consistent modelling of a grain boundary misorientation distribution after equal-channel angular pressing in an AZ31 magnesium alloy. J Mater Sci 48(5):2123–2134
38. Wang H, Wu PD, Tomé CN, Huang Y (2010) A finite strain elastic-viscoplastic self-consistent model for polycrystalline materials. J Mech Phys Solids 58(4):594–612
39. Wang H, Wu PD, Wang J, Tomé CN (2013) A crystal plasticity model for hexagonal close packed (HCP) crystals including twinning and de-twinning mechanisms. Int J Plast 49:36–52
40. Kumar MA, Kanjarla AK, Niezgoda SR, Lebensohn RA, Tomé CN (2015) Numerical study of the stress state of a deformation twin in magnesium. Acta Mater 84:349–358
41. Ardeljan M, Beyerlein IJ, McWilliams BA, Knezevic M (2016) Strain rate and temperature sensitive multi-level crystal plasticity model for large plastic deformation behavior: application to AZ31 magnesium alloy. Int J Plast 83:90–109
42. Feather WG et al (2019) Mechanical response, twinning, and texture evolution of WE43 magnesium-rare earth alloy as a function of strain rate: Experiments and multi-level crystal plasticity modeling. Int J Plast 120:180–204
43. Segurado J, Lebensohn RA, Llorca J, Tomé CN (2012) Multiscale modeling of plasticity based on embedding the viscoplastic self-consistent formulation in implicit finite elements. Int J Plast 28(1):124–140
44. Knezevic M et al (2013) Integration of self-consistent polycrystal plasticity with dislocation density based hardening laws within an implicit finite element framework: application to low-symmetry metals. J Mech Phys Solids 61(10):2034–2046
45. Prakash A, Nöhring WG, Lebensohn RA, Höppel HW, Bitzek E (2015) A multiscale simulation framework of the accumulative roll bonding process accounting for texture evolution. Mater Sci Eng, A 631:104–119
46. Abdolvand H, Daymond MR (2012) Internal strain and texture development during twinning: comparing neutron diffraction measurements with crystal plasticity finite-element approaches. Acta Mater 60(5):2240–2248
47. Abdolvand H, Daymond MR (2013) Multi-scale modeling and experimental study of twin inception and propagation in hexagonal close-packed materials using a crystal plasticity finite element approach; part II: local behavior. J Mech Phys Solids 61(3):803–818
48. Shade PA et al (2019) Exploring new links between crystal plasticity models and high-energy X-ray diffraction microscopy. Current Opin Solid State Mater Sci 23(5):100763
49. Abdolvand H, Majkut M, Oddershede J, Wright JP, Daymond MR (2015) Study of 3-D stress development in parent and twin pairs of a hexagonal close-packed polycrystal: part I–in-situ three-dimensional synchrotron X-ray diffraction measurement. Acta Mater 93:246–255
50. Abdolvand H, Majkut M, Oddershede J, Wright JP, Daymond MR (2015) Study of 3-D stress development in parent and twin pairs

of a hexagonal close-packed polycrystal: part II—crystal plasticity finite element modeling. Acta Mater 93:235–245
51. Pagan DC et al (2017) Modeling slip system strength evolution in Ti-7Al informed by in-situ grain stress measurements. Acta Mater 128:406–417
52. Wang L et al (2018) Study of slip activity in a Mg-Y alloy by in situ high energy X-ray diffraction microscopy and elastic viscoplastic self-consistent modeling. Acta Mater 155:138–152
53. Greeley D, Yaghoobi M, Pagan D, Sundararaghavan V, Allison J (2019) Using synchrotron radiation to improve understanding of deformation of polycrystalline metals by measuring, modelling and publishing 4D information. IOP Conf Ser Mater Sci Eng 580:012017
54. Bieler TR, Wang L, Beaudoin AJ, Kenesei P, Lienert U (2014) In situ characterization of twin nucleation in pure Ti using 3D-XRD. Metall and Mater Trans A 45(1):109–122
55. Lind J et al (2014) Tensile twin nucleation events coupled to neighboring slip observed in three dimensions. Acta Mater 76:213–220
56. Abdolvand H, Majkut M, Oddershede J, Wright JP, Daymond MR (2015) Study of 3-D stress development in parent and twin pairs of a hexagonal close-packed polycrystal: part II–crystal plasticity finite element modeling. Acta Mater 93:235–245
57. Wang L et al (2017) Direct measurement of critical resolved shear stress of prismatic and basal slip in polycrystalline Ti using high energy X-ray diffraction microscopy. Acta Mater 132:598–610
58. Sutton MA, Li N, Joy DC, Reynolds AP, Li X (2007) Scanning electron microscopy for quantitative small and large deformation measurements part I: SEM imaging at magnifications from 200 to 10,000. Exp Mech 47(6):775–787
59. Sutton MA et al (2007) Scanning electron microscopy for quantitative small and large deformation measurements part II: experimental validation for magnifications from 200 to 10,000. Exp Mech 47(6):789–804
60. Kammers AD, Daly S (2013) Digital image correlation under scanning electron microscopy: methodology and validation. Exp Mech 53(9):1743–1761
61. Martin G, Sinclair CW, Lebensohn RA (2014) Microscale plastic strain heterogeneity in slip dominated deformation of magnesium alloy containing rare earth. Mater Sci Eng, A 603:37–51
62. Githens A et al (2020) Characterizing microscale deformation mechanisms and macroscopic tensile properties of a high strength magnesium rare-earth alloy: a combined experimental and crystal plasticity approach. Acta Mater 186:77–94
63. Paudel Y et al (2020) Characterization and modeling of 101¯2 twin banding in magnesium. Acta Mater 183:438–451
64. Ganesan S et al (2021) The effects of heat treatment on the response of WE43 Mg alloy: crystal plasticity finite element simulation and SEM-DIC experiment. Int J Plast 137:102917
65. Qiao H, Agnew SR, Wu PD (2015) Modeling twinning and detwinning behavior of Mg alloy ZK60A during monotonic and cyclic loading. Int J Plast 65:61–84
66. Wu PD, Guo XQ, Qiao H, Lloyd DJ (2015) A constitutive model of twin nucleation, propagation and growth in magnesium crystals. Mater Sci Eng, A 625:140–145
67. Chen Z, Daly S (2018) Deformation twin identification in magnesium through clustering and computer vision. Mater Sci Eng, A 736:61–75
68. Chen Z et al (2018) High-resolution deformation mapping across large fields of view using scanning electron microscopy and digital image correlation. Exp Mech 58(9):1407–1421
69. Chen Z, Daly S (2020) Automated identification of deformation twin systems in Mg WE43 from SEM DIC. Mater Charact 169:110628
70. Yaghoobi M et al (2021) PRISMS-Fatigue computational framework for fatigue analysis in polycrystalline metals and alloys. npj Comput Mater 7(1):1–12
71. Kammers AD, Daly S (2013) Self-assembled nanoparticle surface patterning for improved digital image correlation in a scanning electron microscope. Exp Mech 53(8):1333–1341
72. Githens A, Daly S (2017) Patterning corrosion-susceptible metallic alloys for digital image correlation in a scanning electron microscope. Strain 53(1):e12215
73. Voyiadjis G, Yaghoobi M (2019) Size effects in plasticity: from macro to nano. Academic Press
74. Christian JW, Mahajan S (1995) Deformation twinning. Prog Mater Sci 39(1–2):1–157
75. Kondo R, Tadano Y, Shizawa K (2014) A phase-field model of twinning and detwinning coupled with dislocation-based crystal plasticity for HCP metals. Comput Mater Sci 95:672–683
76. Liu C et al (2018) An integrated crystal plasticity–phase field model for spatially resolved twin nucleation, propagation, and growth in hexagonal materials. Int J Plast 106:203–227
77. Liu G, Mo H, Wang J, Shen Y (2021) Coupled crystal plasticity finite element-phase field model with kinetics-controlled twinning mechanism for hexagonal metals. Acta Mater 202:399–416
78. Ma R, Sun W (2021) Phase field modeling of coupled crystal plasticity and deformation twinning in polycrystals with monolithic and splitting solvers. Int J Numer Meth Eng 122(4):1167–1189